Systematic Design and Experimental Demonstration of Transmission-Type Multiplexed Acoustic Meta-holograms

Yifan Zhu, Nikhil Jrk Gerard, Xiaoxing Xia, Grant Stevenson, Liyun Cao, Shiwang Fan, Christopher Spadaccini, Yun Jing, B. Assouar

Systematic Design and Experimental Demonstration of Transmission-type Multiplexed Acoustic Meta-holograms

Yifan Zhu[†], Nikhil JRK Gerard[†], Xiaoxing Xia, Grant C. Stevenson, Liyun Cao, Shiwang Fan, Christopher M. Spadaccini, Yun Jing[*], and Badreddine Assouar[*]

Dr. Yifan Zhu, Liyun Cao, Shiwang Fan, Prof. Badreddine Assouar
Institut Jean Lamour, Université de Lorraine, CNRS, Nancy, 54000, France
E-mail : badreddine.assouar@univ-lorraine.fr

Dr. Nikhil JRK Gerard, Grant C. Stevenson, Prof. Yun Jing
Department of Mechanical and Aerospace Engineering, North Carolina State University, Raleigh, North Carolina 27695, USA

Dr. Nikhil JRK Gerard, Prof. Yun Jing
Graduate Program in Acoustics, The Pennsylvania State University, University Park, Pennsylvania, 16802, USA
E-mail: yqj5201@psu.edu

Dr. Xiaoxing Xia, Dr. Christopher M. Spadaccini
Lawrence Livermore National Laboratory, 7000 East Avenue, Livermore, California, 94550, USA

[†] Y.F.Z. and N.J.G. contributed equally to this work.

[*] Correspondence to: yqj5201@psu.edu (Y.J.) and badreddine.assouar@univ-lorraine.fr (B.A.)

Keywords: multiplexing, acoustic metamaterials, acoustic metasurfaces, acoustic hologram, amplitude and phase modulations, transmitted waves

Abstract

Acoustic holograms have promising applications in sound-field reconstruction, particle manipulation, ultrasonic haptics and therapy. This paper reports on the theoretical, numerical, and experimental investigation of multiplexed acoustic holograms at both audio and ultrasonic frequencies via a rationally designed transmission-type acoustic metamaterial. The proposed meta-hologram is composed of two Fabry-Pérot resonant channels per unit cell, which enables the simultaneous modulation of the transmitted amplitude and phase at two desired frequencies. In contrast to conventional acoustic metamaterial-based holograms, the design strategy proposed here, provides a new degree of freedom (frequency) that can actively tailor holograms that are otherwise completely passive and hence significantly enhances the information encoded in acoustic metamaterials. To demonstrate the multiplexed acoustic metamaterial, we first show the projection of two different high-quality meta-holograms at 14 kHz and 17 kHz, with the patterns of the letters, N and S. We then demonstrate two-channel ultrasound focusing and annular beams generation for the incident ultrasonic frequencies of 35 kHz and 42.5 kHz. These multiplexed acoustic meta-holograms offer a technical advance to tackle the rising challenges in the fields of acoustic metamaterials, architectural acoustics, and medical ultrasound.

1. Introduction

Drawing inspiration from their optical counterparts, acoustic holograms have been recently reported [1-9], and now offer fresh perspectives on a wide-range of applications like advanced sound-field reconstruction, ultrasonic therapy, haptics, and particle manipulation. In this regard, transducer arrays [2-4], monolithic phase plates [5], and acoustic metamaterials/metasurfaces [6-9] are often frequent candidates for the generation of holographic images that possess unique

features and functionalities. Conventional approaches [1-6] are largely based on pure phase surface and therefore necessitate iterative computational optimization, such as the Gerchberg–Saxton algorithm [6]. Despite this, such approaches are still accompanied by sub-optimal image quality since the simultaneous modulation of both amplitude and phase is crucial for the reconstruction of high-precision wave fields.

To address this limitation, some recent studies have demonstrated that metasurfaces equipped with precise control over both phase and amplitude could offer a promising route for high-fidelity acoustic holography [7-11]. Metasurfaces [11-20] are two-dimensional materials of sub-wavelength thickness that enable unconventional wavefront shaping functionalities due to their carefully engineered metamaterial [21-26] structural units. In a prior study, it was illustrated that reflection-type lossy acoustic metamaterials (LAM) [8] could facilitate decoupled amplitude and phase modulation (APM) and therefore allow for the realization of high-quality images that were previously unattainable. Further, a major advantage is that a straightforward, deterministic time-reversal approach could be employed for the calculation of the required APM profile, and hence ensures high accuracy and bypasses the need for complex computational optimization.

Meanwhile, the past few years have also witnessed the advent of multiplexed optical metasurface-based holograms which are encoded with several predesigned patterns or functionalities, that can be selectively projected on to image planes based on the helicity [27, 28], angle [29], frequency [30, 31] or the direction [32] of the incident wave. Similarly, our recent paper [33] put forward the concept for a reflection-type multiplexed acoustic metamaterial (RMAM) that enables high-fidelity frequency dependent holograms for audible sound. Each unit cell of the RMAM comprises multiple Helmholtz resonators (HRs) [34-37] that are tuned to distinct operating frequencies. These HRs hence possess the geometrical entities that can be

utilized to precisely control the amplitude and phase responses at each of these frequencies independently. Although both LAM and RMAM give rise to advanced routes for acoustic holography, these concepts have remained limited to reflective metamaterials in the audible regime. Multiplexing for transmitted wave meta-hologram, on the contrary, holds great potential for a wider range of acoustic wave-based applications as the interference between the hologram and the incident wave is substantially reduced.

Extending prior designs to transmission-based systems, however, is a challenging problem for both optics and acoustics and has hence rendered all prior frequency multiplexed optical [30, 31] and acoustical [35] meta-holograms to be of reflection-type. In acoustics, a single HR is insufficient to induce and tailor the required non-trivial local phase shift for transmitted waves and therefore implies more complicated geometries [38]. These are particularly cumbersome to fabricate for higher operating frequencies, where the feature sizes of the micro-structure are much smaller. Additionally, the amplitude modulation in the LAM and RMAM designs is made possible by artificially introducing loss in a controlled manner via leaky slits and absorbing boundaries, that are unfeasible in the case of transmission. New strategies for transmission-type multiplexed metamaterials are thus highly desirable, in order to advance acoustic holography across a broad range of frequencies.

In this paper, we put forward transmission-type multiplexed acoustic meta-holograms (MAMH) and experimentally illustrate their working for both audible sound and ultrasound. The physical mechanism hinges on unit cells that consist of multiple Fabry-Pérot (FP) resonant channels [39, 40], whose effective heights correspond to the distinct operating frequencies of interest. Each of these FP resonant channels in turn consists of amplitude and phase modulating sub-structures that allow for precise and simultaneous APM. Furthermore, the amplitude

modulation in this case, is made possible by elegantly engineering the inherent dissipation that exists in the sub-wavelength FP channels owing to the thermal and viscous boundary layer effects [41-43]. This is highly beneficial for ultrasonic applications, where thermo-viscous losses are very high and are at present deemed extremely undesirable [44, 45]. We employ a two-channel version of our unit cell to systematically design and illustrate frequency dependent functionalities that leverage simultaneous APM and significantly increase the degrees of freedom for conventional acoustic wave manipulation. To this end, we demonstrate multiplexed high-quality audio holography at 14 kHz and 17 kHz, and two-channel ultrasonic focusing and frequency dependent ultrasonic annular beam generation at 35 kHz and 42.5 kHz. We choose these two groups of frequencies, not farther apart (viz. $f_2 \approx 1.2f_1$), in order to demonstrate that the strategy that we employed is efficient in decoupling the responses of the two frequencies, even though they are close together. These demonstrations could pave the way for a host of multiplexed and switchable compact devices that could facilitate various applications in room acoustics, audio engineering, virtual reality, and biomedical ultrasound.

2. Results

2.1. Working Principle of the MAMH

Figures 1a, **b** illustrate the working principle of the MAMH, where the incident wavefront consists of two frequencies, *viz*., f_1 and f_2, marked by the green and blue arrows, respectively. For multiplexed transmission holography, when the wave propagates through the MAMH, it must be reshaped such that it projects different predesigned images for f_1 and f_2, on to an image plane that exists at a given distance in front of it. The desired holographic patterns can be arbitrarily chosen and captured by the acoustic pressure field, denoted here by, $P_n(x, y, z)$, where n corresponds to

the operating frequency (n = 1 or 2 in this study). In order to reconstruct this image via a meta-hologram, we first employ the time-reversal (TR) method [8] to calculate the pressure profile, $p_n(x_j, y_j)$, that must exist at the hologram plane. We then design the meta-hologram such that it facilitates an amplitude and phase distribution, $(A_{n(\mathrm{TR})}, \varphi_{n(\mathrm{TR})})$, that is consistent with $p_n(x_j, y_j)$ on the hologram plane and therefore satisfies the desired $P_n(x, y, z)$ at the image plane for the n^{th} frequency.

Foremost, $P_n(x, y, z)$ is decomposed into a collection of pixels that are represented in Figure 1a, by $p_n(x_l, y_l, z_l)$, where l denotes the pixel number. The pressure at each of the l^{th} pixels can in turn be defined as, $p_n(x_l, y_l, z_l) \equiv p_l \equiv A_{0l}\exp(i\varphi_{0l})$, where A_{0l} and φ_{0l} are the predesigned amplitude and phase of a pixel that is located at a point, (x_l, y_l, z_l), on the image plane. In hologram design, we usually set $\varphi_{0l} = 0$, which means that the phase distribution of the predesigned image is uniform. Likewise, the hologram plane can be described by a collection of pixels, and the pressure at every j^{th} pixel can be written as, $p_n(x_j, y_j) \equiv p_j \equiv A_j\exp(i\varphi_j)$ with amplitude A_j and phase φ_j. Since the system obeys time-reversal symmetry, A_j and φ_j, can be calculated by simply back projecting the information on the image plane as follows,

$$p_j = \sum_{l=1}^{N} \frac{A_{0l}}{r_l} \exp[i(k_n r_l + \phi_{0l})], \tag{1}$$

where $k_n = 2\pi f_n/c_0$ is the wave number, c_0 = 343 m/s is the sound speed in air. N is the total number of image pixels, and the distance, r_l , between the image pixel and hologram pixel can be calculated as, $r_l^2 = (x_j\text{-}x_l)^2+(y_j\text{-}y_l)^2+(z_j\text{-}z_l)^2$. Similarly, by employing the values of p_j, we can reaffirm its accuracy by analytically calculating the pressure distribution at the image plane through the following formula

$$P_n(x,\ y,\ z) = \sum_{j=1}^{M} \frac{A_j}{r_j} \exp[-i(k_n r_j - \phi_j)], \tag{2}$$

where M is the total number of hologram pixels and the distance, r_j, between the spatial point at (x, y, z) and the hologram pixel, (x_j, y_j, z_j), satisfies, $r_j^2 = (x-x)^2+(y-y_j)^2+(z-z_j)^2$. The calculated values of A_j and φ_j, obtained from Eq. (1), would hence serve as the required values of ($A_{n(\mathrm{TR})}$, $\varphi_{n(\mathrm{TR})}$) and can be arranged as a function of x and y in order to realize multiplexed holography.

It is quite evident from the above, that an MAMH must possess structural units that are endowed with complete control over the amplitude and phase of the transmitted wave, at each of these frequencies independently. Therefore, in what follows, we first delineate the design of our unit cell for the target audio frequencies, f_1 = 14 kHz, and f_2 = 17 kHz, and then couple this with the aforementioned technique to demonstrate high-precision frequency dependent holography at f_n. The latter part of the paper will then put forward the extension of this design to the ultrasonic regime and the subsequent realization of two-channel focusing and annular beam generation.

2.2 Unit Cell Design

The MAMH is made up of 3D unit cells with multiple resonant sub-units, as shown in Figure 1c. Each unit cell has two FP resonant channels [39, 40], which are denoted here by C_1 and C_2 for channels 1 and 2, respectively. The structure of the channels is made by a solid material and the background medium is air. The size of the unit cell is 10 mm × 10 mm × 45 mm and the transverse dimensions are smaller than half the wavelength for both cases (i.e., λ_1 = 24.5 mm, λ_2 = 20.2 mm). It ensures that only the fundamental mode propagates, independent of the angle of incidence. Further, as illustrated in Figure 1c, the unit cell comprises frequency, amplitude, and phase modulators, *viz.*, the FM, AM, and PM, that are marked in blue, black, and red, respectively.

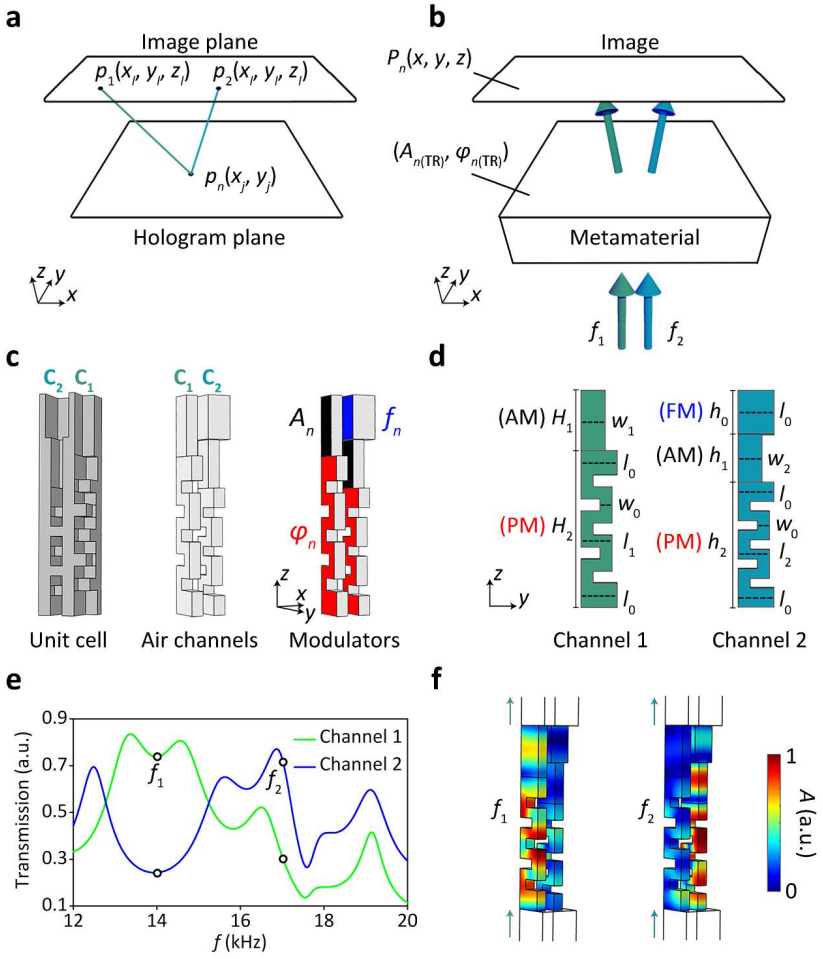

Figure 1. The schematic diagram of MAMH. (a) The schematic diagram of the hologram plane and image plane. (b) The schematic diagram of the MAMH that can generate two different images at two frequencies f_1 and f_2. (c) The unit cells consist of two channels (1 and 2) corresponding to two Fabry–Pérot resonant frequencies, f_1 and f_2. The figures show the 3D structure of the unit cell and the background medium of the air channel. The schematic diagram of the unit cell consisting of three modulators, *viz.*, the frequency modulator (FM), amplitude modulator (AM) and phase modulator (PM) marked by blue, black and red, respectively. (d) The 2D structure of C_1 and C_2. The parameters are marked in the figure. (e) The transmission curves of C_1 and C_2 from 12 kHz to 20 kHz with $w_1 = w_2 = 7.5$ mm, $l_1 = l_2 = 7.5$ mm. At f_1=14 kHz (green line), the transmission of C_1 is much higher than C_2. At $f_2 = 17$ kHz (blue line), the transmission of C_2 is much higher than C_1. (f) The acoustic pressure amplitude fields in the unit cells at $f_1 = 14$ kHz and $f_2 = 17$ kHz, respectively. The arrows indicate the incident and transmitted directions.

Figure 1d shows the 2D cross-section of C_1 and C_2, along with the relevant geometrical parameters. C_1 is composed of AM and PM regions with heights $H_1 = 12.5$ mm and $H_2 = 32.5$

mm, respectively. The total height of the two regions, H, is therefore the height of the entire unit cell ($H = H_1 + H_2 = 45$ mm). The AM is an air-channel on the top that has a width, w_1, which can be tailored to be between 3 mm and 8 mm to predominantly modulate the amplitude of the transmitted wave. The PM is a zig-zag channel whose total effective length can be controlled by tuning the parameter l_1 between 3 mm and 8 mm and modulates the transmitted phase. The width of this zig-zag channel, $w_0 = 2.5$ mm and its top and bottom are connecting channels with a fixed width of $l_0 = 7.5$ mm. The two parameters (w_0, l_0) were optimized to make the tunable range of the PM large enough, so as to facilitate a wide span of local phase shifts.

To start with, we first design C_1 by matching its resonance frequency to the first desired working frequency, f_1 =14 kHz. This is done by choosing the values of H_1 and H_2 such that its sum satisfies the FP resonance condition for f_1. Here, the total height of the unit cell, H, is chosen to be approximately twice the first work working wavelength, i.e., $H \approx 2c_0/f_1$. The C_2 is then designed by including a wider air channel, on top of the AM, that matches well with the impedance of the free space. This wider channel is defined as FM, because its height $h_0 = (1-\beta)H$ is changed to choose the second targeted frequency. Here, the β is a factor of reduction that is applied to the heights of the AM and PM via $h_1 = \beta H_1$ and $h_2 = \beta H_2$ respectively and allows us to tailor the frequency at which the FP resonance of C_2 occurs. In this case, we search the value of β and set $\beta = 0.8$, so that the heights of the FM, AM and PM are $h_0 = 9$ mm, $h_1 = 10$ mm, and $h_2 = 26$ mm, respectively, and the FP resonance for the C_2 (which corresponds to $h_1 + h_2$) occurs at the second desired working frequency, $f_2 = 17$ kHz. It is also useful to note here that, $\beta \approx f_1/f_2$, due to the fact that the resonant wavelength of the acoustic meta-materials can be approximately scaled up with the structural size [21-23]. For more elaborate analytical and descriptive details about the unit cell, the reader is referenced to Supporting Information Note 1.

The properties of the conceived sub-units were then assessed by numerically calculating the transmission curves for C_1 and C_2, in the frequency range between 12 and 20 kHz, with $w_1 = w_2 = 7.5$ mm, $l_1 = l_2 = 7.5$ mm. These results are shown in Figure 1e and illustrate that at f_1, the transmission through C_1 (0.74) is much higher than that of C_2 (0.24). Likewise, at f_2, the transmission of C_2 (0.73) is much higher than C_1 (0.31). Further, Figure 1f shows the acoustic pressure amplitude field through a unit cell made up of these channels, at f_1 and f_2, respectively. It can be clearly seen here that when f_1 (f_2) is incident, the response from C_1 (C_2) is dominant and that of C_2 (C_1) results in a very low amplitude background noise. This verifies our theory that the two-channel FP resonance mechanism allows for frequency selective wave transmission with a negligible background noise. Additionally, the transmitted amplitude (A) and phase (φ) for each frequency can be calculated as a function of the different geometrical parameters of C_1 and C_2, respectively. **Figures 2**a, b show the various (A_1, φ_1) and (A_2, φ_2), that can be achieved by modulating the geometrical parameters (w_1, l_1) and (w_2, l_2), for f_1 and f_2, respectively. It is interesting to note here, that the numerical calculations employed take into consideration the thermo-viscous dissipation that exists in these channels and contribute to the amplitude modulation that is achieved. A design library was then built for these working frequencies, with 4 discrete values of amplitude and 8 of phase. The 4 values of amplitude that were chosen are 0.32, 0.48, 0.64, and 0.8 and were normalized to 0.4, 0.6, 0.8, and 1, respectively. The values of phase were discretized between $\pi/4$ and 2π, with a step size of $\pi/4$. These 4×8 combinations are shown in Figures 2c, d and have (w_1, l_1) and (w_2, l_2) dimensions that both lie between 3 mm and 8 mm, with a step size of 0.5 mm between them. Therefore, a MAMH that comprises these unit cells can be conveniently realized via a commercial extrusion-based 3D printer. (For additional details about the amplitude and phase library, the reader is referenced to Supporting Information

Note 1)

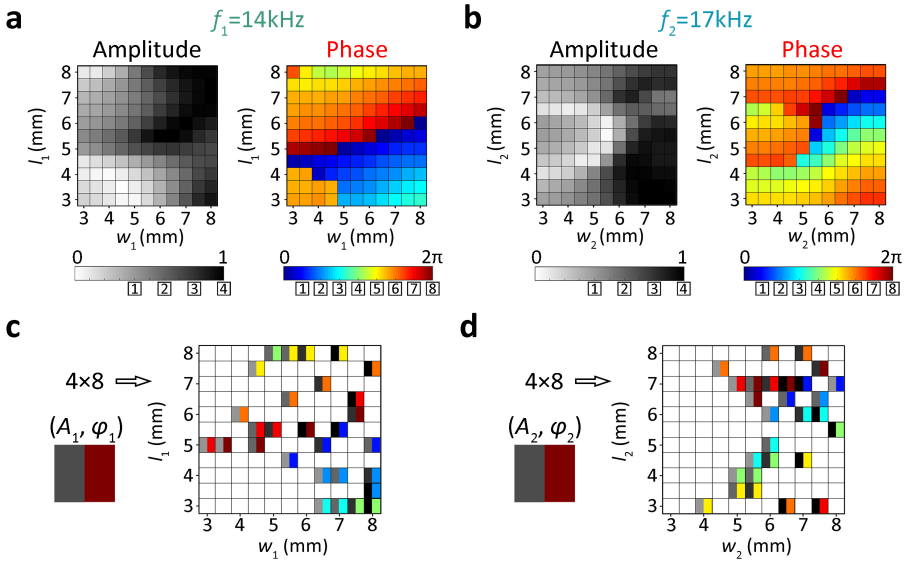

Figure 2. Amplitude and phase responses of the unit cell for 14 kHz and 17 kHz. (a) The amplitude and phase responses as a function of the parameters w_1 and l_1 for $f_1 = 14$ kHz. (b) The 4×8 combinations of (A_1, φ_1) varying with w_1 and l_1. (c) The amplitude and phase responses varying with parameters w_2 and l_2 for $f_2 = 17$ kHz. (d) The 4 × 8 combinations of (A_2, φ_2) varying with w_2 and l_2.

2.3 High-Fidelity Multiplexed Audio Holography

The aforementioned methods were then employed to design a meta-hologram that could selectively project the letters N and S for f_1 = 14 kHz and f_2 = 17 kHz, respectively, on to an image plane that sits 5 cm away (z_l = 5 cm) from the hologram plane (z_j = 0 cm), as shown in **Figure 3**a. The source employed in our experiments was a loudspeaker of diameter 10 cm that was placed 10 cm behind the sample. This was hence regarded as a point source in the full-wave numerical simulations, and the associated amplitude and phase compensation, (A_{source}, φ_{source}) were incorporated in our design to improve its experimental accuracy. This was done by adding a compensation to $A_{n(\mathrm{TR})}$ and $\varphi_{n(\mathrm{TR})}$, to obtain the final amplitude, $A_n = A_{n(\mathrm{TR})}/A_{source}$ and phase, $\varphi_n = \varphi_{n(\mathrm{TR})}-\varphi_{source}$. Figure 3b shows the amplitude, $A_{n(\mathrm{TR})}$, and phase, $\varphi_{n(\mathrm{TR})}$, distributions that were

calculated by time-reversal for the holographic rendering of the letters, N and S. The plots adjacent to them, A_n and φ_n, represent the corrected values of the same, upon including the source compensation. The final amplitude and phase profiles that were used for the final MAMH, are shown in Figure 3c as a function of x and y. One might note here that the designed images are at two different locations (two adjacent regions). This was done to minimize the coupling between the two working frequencies, and to ensure images with highest fidelity and lowest background noise.

The design library put forward in the previous section was then revisited to obtain the dimensions for a set of 17 × 17 unit cells that could build the desired MAMH sample of size 18 cm × 18 cm × 4.5 cm (including wall thickness). Figure 3d shows the 3D printed prototype of the MAMH that was experimentally characterized by mapping the field over a 20 cm × 20 cm region, at z = 5 cm. **Figures 4**a, b present the simulated and measured acoustic intensity distributions on the transmissive side of the metamaterial for both frequencies of incidence. The arrows in Figure 4a, indicate the direction of propagation and show the numerically calculated intensity field at z = 4 cm, 5 cm, and 6 cm away from the sample. The letters 'N' and 'S' are distinctly visible for the two cases and are unimpaired when z = 5 cm, proving that the performance of the sample is consistent with our conceived design. Figure 4b also shows that the measured acoustic intensity field at z = 5 cm, agrees very well with the simulation results and validates the ability of the MAMH to generate high-quality frequency dependent holograms, owing to its simultaneous APM and multiple FP resonance-based mechanism. This unique capability could enable new audio devices and also greatly help renovate existing applications like stereo-sound field reconstruction [46]. It is possible that some undesirable effects could arise due to the coupling between the different unit cells and the interaction between the transmitted acoustic waves and

the sufficient number of channels. Although the theoretical calculations here did not take this coupling into account, the fact that the numerical results agree well with the theoretical predications is indicative of these interactions being rather trivial in this case.

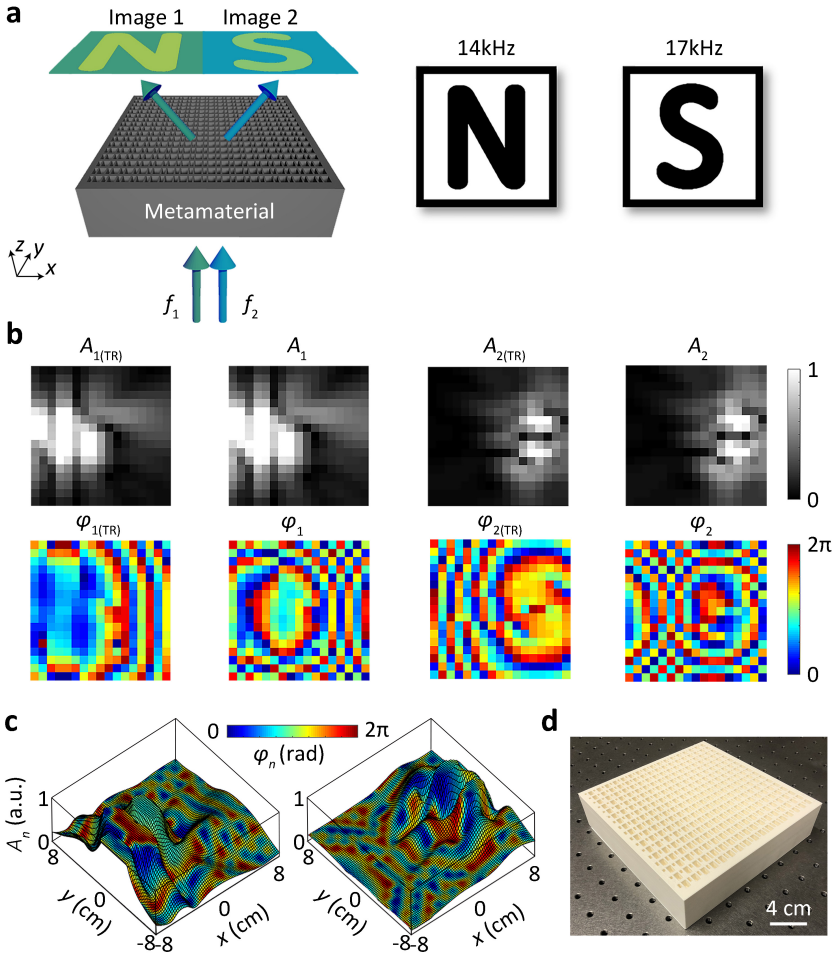

Figure 3. The holographic designs for letters "N" and "S" at 14 kHz and 17 kHz. (a) The predesigned holographic image at 14 kHz is letter "N". The image plane is 5 cm away (z = 5 cm) from the hologram plane. (b) The amplitude and phase distributions at hologram plane calculated by time reversal are ($A_{n(\mathrm{TR})}$, $\varphi_{n(\mathrm{TR})}$). The final amplitude and phase distributions of the sample are calculated as (A_n, φ_n). (c) The final distributions of (A_1, φ_1) and (A_2, φ_2). (d) The photograph of the sample with a size of 18 cm × 18 cm × 4.5 cm with 17 × 17 unit cells. Scale bar, 4 cm.

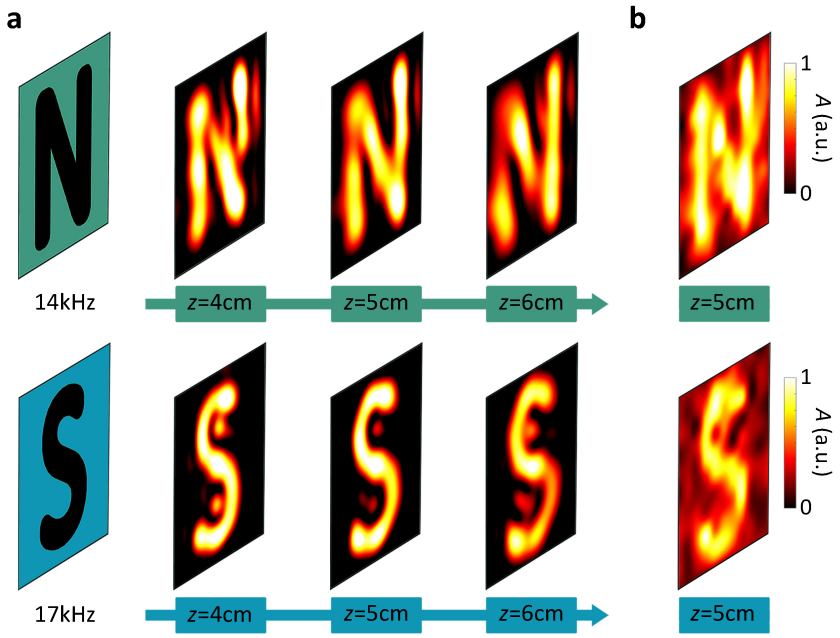

Figure 4. Simulated and experimental results of holographic images (letter "N") at 14 kHz and (letter "S") at 17 kHz. (a) The simulated acoustic intensity distributions at the distance of z = 4 cm, z = 5 cm, z = 6 cm, respectively. The arrows indicated the wave is propagating along the z-direction. (b) The measured acoustic intensity distributions at the predesigned image plane of z = 5 cm.

2.4 Frequency Dependent Ultrasonic Holography

The principle and design of our meta-hologram can also be readily extended to operate at ultrasonic frequencies. This is of interest, since multiplexing could greatly benefit ultrasonic applications like therapy and particle manipulation, by circumventing the need for bulky and expensive phased array systems that currently serve as the state of the art for ultrasound beam forming. Besides, the strong intrinsic thermo-viscous loss in ultrasonic metamaterials would facilitate the amplitude modulation that is highly desirable for the MAMH design that is proposed here. The experimental realization of such an ultrasonic meta-hologram would thus greatly bolster the interest for high precision miniaturized acoustic wave-based devices. **Figures 5**a, b show the amplitude and phase responses for our unit cell when it is scaled down by a factor

of 0.4. The unit cell now has the dimensions 4 mm × 4 mm× 1.8 mm, and the frequencies of incidence are modified to f_1 = 35 kHz and f_2 = 42.5 kHz. The design library was built as done previously, with 4 × 8 combinations of A_1 and φ_1 (A_2 and φ_2) with w_1 (w_2) and l_1 (l_2) now varying between 1.2 mm and 3.2 mm, with a step size of 0.2 mm, as shown in Figures 5c, d. (Additional details in this regard can be found in Supporting Information Notes 1 and 2) This unit cell library was then leveraged to design two multiplexed ultrasonic meta-holograms (MUMH) for the functionalities of frequency dependent focusing and annular beam generation, respectively.

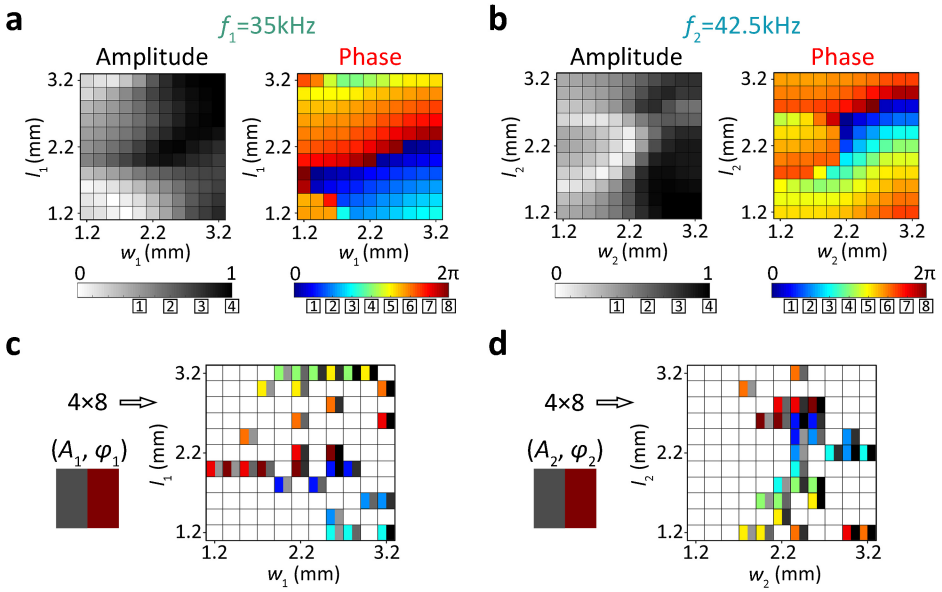

Figure 5. Amplitude and phase responses of the unit cell for 35 kHz and 42.5 kHz. (a) The amplitude and phase responses changing with parameters w_1 and l_1 for f_1 = 35 kHz. (b) The 4 × 8 combinations of (A_1, φ_1) varying with w_1 and l_1. (c) The amplitude and phase responses varying with parameters w_2 and l_2 for f_2 = 42.5 kHz. (d) The 4 × 8 combinations of (A_2, φ_2) changing with w_2 and l_2.

Figure 6a shows the schematic for an MUMH that acts as a two-channel ultrasonic lens [47] which exhibits frequency dependent focusing on an image plane that is 1 cm away (z_I = 1 cm). The predesigned holographic images in this case are that of focal points that exist at two different

corners of the image plane i.e. (-1.1 cm, 1.1 cm, 1 cm) and (1.1 cm, -1.1 cm, 1 cm), for f_1 and f_2, respectively. Figure 6b here shows the required amplitude and phase distributions that were calculated by the method described earlier. To enable this frequency dependent pressure profile, the MUMH sample was designed with an appropriate set of 10 × 10-unit cells and was fabricated by a commercial high-resolution stereolithography based 3D printer. The resultant prototype of size 4.8 cm × 4.8 cm × 1.8 cm (including wall-thickness) is shown in Figure 6c. To experimentally illustrate its working, an air-coupled ultrasonic transducer of diameter 1 cm (center frequency 40 kHz), was placed well-behind the sample (i.e. in the far-field, approx. 5 cm away) such that the wavefront that impinges on the MUMH has a uniform phase distribution and could be captured by a plane wave incidence in the full-wave simulations. The left panel of Figure 6d shows the numerically calculated pressure amplitude distribution on an image plane of size, 4.8 cm × 4.8 cm, situated in front of the sample at z = 1 cm. It can be clearly seen here that the designed MUMH enables frequency dependent wave focusing that is consistent with the predesigned holographic images show in Figure 6a. This is also evident in our experimentally measured results, shown in the right panel of Figure 6d, which agree well with the numerically calculated ones and thereby validates the functionality of our prototype. To further verify the accuracy of the frequency dependent focusing and to compare the simulations with experiments, as shown in Figure 6e, the pressure amplitude along the diagonal (described by $x + y = 0$, $z = +1$, shown in the inset) of the image plane was calculated. Here, the x axis denotes the distance between the targeted coordinate and the ordinate (0 cm, 0 cm, 1 cm). The curve calculated from the measurement (squares) has a very reasonable agreement with the numerical results (solid line). Our realization of frequency dependent ultrasonic focusing via a meta-hologram, could greatly aid biomedical applications, since high intensity focused ultrasound is now an emerging

candidate for treating different diseases and conditions [48].

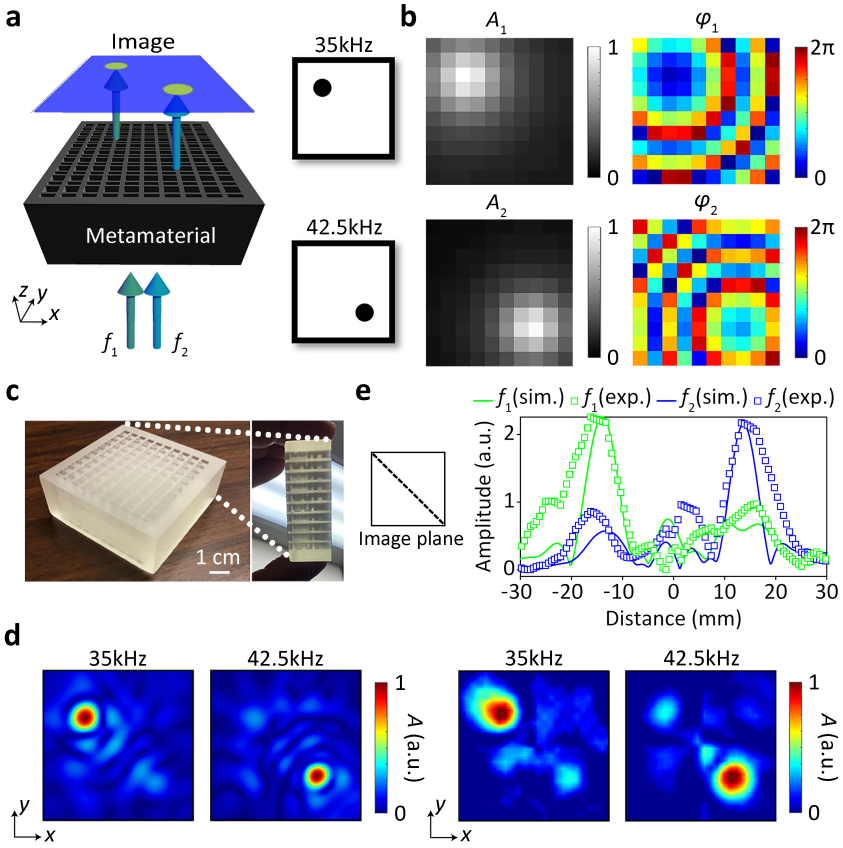

Figure 6. The design and demonstration of two-channel ultrasound lens. (a) The schematic diagram of the MUMH for two-channel ultrasound focusing. The image plane is 1 cm away (z_I = 1 cm) from the hologram plane. The predesigned holography patterns are two focal points at the coordinate (-1.1 cm, 1.1 cm, 1 cm), and (1.1 cm, -1.1 cm, 1 cm), respectively. (b) Calculated amplitude and phase distributions for 35 kHz and 42.5 kHz, respectively. (c) The photograph of the 3-D printing sample, consisting of 10 × 10 unit cells with a size of 4.8 cm × 4.8 cm × 1.8 cm. Scale bar, 1 cm. (d) The simulated (left panel) and the measured (right panel) acoustic pressure amplitude distributions for 35 kHz and 42.5 kHz, respectively. Scale bar, 1 cm. (e) The simulated (sim., green and blue lines) and experimental (exp., green and blue squares) acoustic pressure amplitude distributions along the diagonal $x + y = 0$, $z = +1$ (shown in the inset). The horizontal axis is the distance between the targeted coordinate and the ordinate (0 cm, 0 cm, 1 cm).

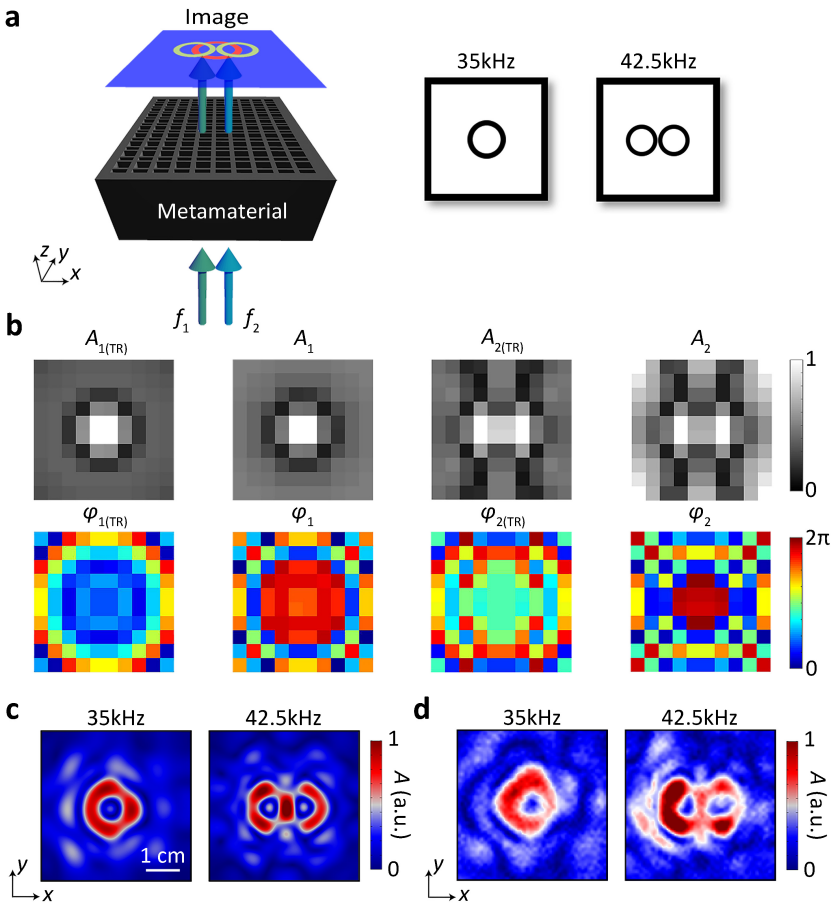

Figure 7. The design and demonstration of two-channel annular beams. (a) The schematic diagram of the MUMH for annular beams. The image plane is 1 cm away (z_l = 1 cm) from the hologram plane. The predesigned holography pattern for f_1 = 35 kHz is one annular beam with the center coordinate (0 cm, 0 cm, 1 cm). The predesigned holography pattern for f_1 = 42.5 kHz is a pair annular beams with the center coordinates (-0.6 cm, 0 cm, 1 cm) and (0.6 cm, 0 cm, 1 cm). (b) The amplitude and phase distributions at hologram plane calculated by time reversal is ($A_{n(TR)}$, $\varphi_{n(TR)}$). The final amplitude and phase distributions of the sample are calculated as (A_n, φ_n). (c) The simulated acoustic pressure amplitude distributions of annular beam in *x*-*y* plane for 35 kHz and 42.5 kHz, respectively. Scale bar, 1 cm. (d) The measured acoustic pressure amplitude distributions of annular beam in *x*-*y* plane.

Additionally, to demonstrate highly precise wave reconstruction at the small wavelengths associated with 35 kHz and 42.5 kHz, we designed an ultrasonic MUMH that could generate distinctive annular beam patterns [48], that are dependent on the frequency of the incident wave. The schematic on **Figure 7**a (left) illustrates the desired MUMH and shows that it would generate a single annular beam which has a center coordinate at (0 cm, 0 cm, 1 cm) when f_1 is

incident, but when f_2 is incident, it would generate two annular beams that have two center coordinates at (-0.6 cm, 0 cm, 1 cm) and (0.6 cm, 0 cm, 1 cm). Figure 7a (right) shows the predesigned images that are taken into consideration in order to project these functionalities on to an image plane at z_l = 1 cm. For this case, the amplitude and phase distributions that were calculated via time-reversal ($A_{n(\mathrm{TR})}$, $\varphi_{n(\mathrm{TR})}$), are shown in Figure 7b for f_1 (left) and f_2 (right), respectively. The single air-coupled transducer was employed here as the source and was placed 3.5 cm behind the sample to ensure a good signal-to-noise ratio. However, since the incident wavefront here is not planar, amplitude and phase compensations were incorporated to the design, as done in the case of the audio meta-hologram, and the resultant (A_n, φ_n), for both frequencies, are shown adjacent to the initially calculated plots in Figure 7b. Figure 7c shows that the numerically predicted acoustic pressure amplitude distribution at the image plane, efficiently captures the details of the predesigned images for both f_1 and f_2. Figure 7d presents the experimentally measured pressure amplitude fields, that agree well with the numerical results and hence confirms that our ultrasonic meta-hologram generates distinctive channel/frequency dependent annular beams, whose centers lie at the desired coordinates. Such frequency dependent annular beam generation via a MUMH is highly desirable for acoustical tweezer-based particle manipulation [50].

3. Conclusion

In summary, we designed and experimentally illustrated the working of multiplexed metamaterials for high fidelity acoustic holographic rendering. A new class of unit cells that could simultaneously modulate the amplitude and phase at two different frequencies were put forward and leveraged to build multiplexed meta-holograms that are encoded to project different predesigned images at different frequencies. The resultant meta-holograms not only introduce

frequency as a new degree of freedom in metamaterial design, but also enable the generation of high-quality audio and ultrasonic wavefront reconstruction without the need for complex computational optimization. As a proof of concept, we numerically and experimentally demonstrated high-grade multiplexed audio holography, frequency dependent ultrasonic focusing, and two-channel annular beam generation. These demonstrated functionalities are benevolent for a wide-range of acoustic applications and could open avenues to next-generation devices for stereo-sound field reconstruction [46], ultrasonic therapy [48], and particle manipulation [50] based on switchable audio and ultrasonic devices.

4. Experimental Section

Numerical Simulations: The simulations were performed using the commercial finite element analysis software, COMSOL Multiphysics 5.5a with the "Acoustic-Thermoviscous, Acoustic Interaction, Frequency Domain". The walls of the solid materials in the unit cells are set as sound hard boundaries. The considered mass density and the sound speed of background medium air are $\rho_0 = 1.21$ kg/m^3 and $c_0 = 343$ m/s, respectively.

Fabrication: The sample for audio holography was fabricated using a commercial extrusion-based 3D printer (Ultimaker 3, feature resolution = 0.25 mm) and the material of poly-lactic acid (PLA). The samples for ultrasound experiments are fabricated using a commercial stereolithography 3D printer (Formlabs Form 3, feature resolution = 0.1 mm) and Formlabs Clear V4 resin. The 3D printed samples were rinsed in IPA in Form Wash for 10min and then post-cured by 405 nm light in Form Cure for 1hr.

Experimental Measurements: The experiments were carried out in a 3D space. For the measurement at 14 kHz and 17 kHz, a 10 cm-diameter loudspeaker was fixed at the incident side of the sample with a distance of 10 cm. The measurement of the acoustic intensity fields in

Figure 4 are obtained by scanning the output side of the sample with a distance of 5 cm (*viz.*, image plane), via 1/8-inch-diameter Brüel&Kjær type-4138-A-015 microphone and Brüel&Kjær PULSE Type 3160. The scanning area at image plane is 20 cm × 20 cm. For the measurement at 35 kHz and 42.5 kHz (the results for which are shown in Figures 6, 7), an air-coupled ultrasonic transducer (Murata MA40S4S) of 1 cm-diameter was used as the source and placed at a distance, 3.5 cm behind the sample, for the annular beam measurement, and in the far field, for the focusing measurement. On the transmissive side, a GRAS Type 46BF free-field microphone of 1/4 inch diameter was translated by means of a linear scan stage over a square region of size, 4.8 cm × 4.8 cm. The data from the microphone was collected through a GRAS 12AA power module and Picoscope 4824 oscilloscope that helped improve the signal-to-noise ratio and offered a sufficiently high sampling frequency, respectively.

Analytical Derivation: The amplitude and phase response of the unit cell can be analytically deduced by the transfer matrix method. (See Supporting Information Note 3)

Acknowledgements

This work is supported by the Air Force Office of Scientific Research under award number FA9550-18-1-7021, and by la Région Grand Est and Institut Carnot ICEEL. Y. J. would like to thank NSF for the support through CMMI 1951221. Work at LLNL was performed under the auspices of the U.S. Department of Energy by Lawrence Livermore National Laboratory under Contract DE-AC52-07NA27344.

Author Contributions

Y.F.Z and N.J.G. contributed equally to this work. Y.F.Z. and N.J.G. performed the theoretical simulations. Y.F.Z., L.Y.C., S.W.F. and B.A. conceived and designed the experiments for the audio meta-hologram. N.J.G., G.C.S. and Y.J. conceived and designed the experiments for the

ultrasonic meta-holograms. X.X.X. and C.M.S. fabricated the samples for ultrasound. Y.F.Z., N.J.G., Y.J. and B.A. wrote the manuscript. Y.J. and B.A. guided the research. All authors contributed to data analysis and discussions.

Conflict of Interest

All authors declare that they have no conflict of interest.

Supporting Information

Supporting Information is available from the Wiley Online Library or from the author.

References

[1] Y. Hertzberg, G. Navon, *Med. Phys.* **2011**, *38*, 6407–6415.

[2] A. Marzo, S. Seah, B. Drinkwater, D. Sahoo, B. Long, S. Subramanian, *Nat. Commun.* **2015**, *6*, 8661.

[3] A. Marzo, B. W. Drinkwater, *Proc. Natl. Acad. Sci.* **2019,** *116*, 84-89.

[4] R. Hirayama, D. M. Plasencia, N. Masuda, S. Subramanian, *Nature* **2019,** *116*, 320–323.

[5] K. Melde, A. G. Mark, T. Qiu, P. Fischer, *Nature* **2016,** *537*, 518–522.

[6] Y. Xie, C. Shen, W. Wang, J. Li, D. Song, B-I, Popa, Y. Jing, S. A. Cummer, *Sci. Rep.* **2016,** *6*, 35437.

[7] Y. Tian, Q. Wei, Y. Cheng, X. J. Liu, *Appl. Phys. Lett.* **2017,** *110*, 191901.

[8] Y. F. Zhu, J. Hu, X. D. Fan, J. Yang, B. Liang, X. F. Zhu, J. C. Cheng, *Nat. Commun.* **2018**, *9*, 1632.

[9] S. W. Fan, Y. F. Zhu, L. Y. Cao, Y. F. Wang, A. L. Chen, A. Merkel, Y. S. Wang, B. Assouar, *Smart Mater. Struct.* **2020,** *29*, 105038.

[10] R. Ghaffarivardavagh, J. Nikolajczyk, R. G. Holt, S. Anderson, X. Zhang, *Nat. Commun.* **2018,** *9*, 1349.

[11] B. Assouar, B. Liang, Y. Wu, Y. Li, J. C. Cheng, Y. Jing, *Nat. Rev. Mater.* **2018,** *3*, 460–472.

[12] Y. Li, B. Liang, Z. M. Gu, X. Y. Zou, J. C. Cheng, *Sci. Rep.* **2013**, *3*, 2546.

[13] G. C. Ma, M. Yang, S. W. Xiao, Z. Y. Yang, P. Sheng, *Nat. Mater.* **2014**, *13*, 873.

[14] Y. B. Xie, W. Q. Wang, H. Y. Chen, A. Konneker, B. I. Popa, S. A. Cummer, *Nat. Commun.* **2014**, *5*, 5553.

[15] X. F. Zhu, K. Li, P. Zhang, J. Zhu, J. T. Zhang, C. Tian, S. C. Liu, *Nat. Commun.* **2016**, *7*, 11731.

[16] C. Shen, Y. Xie, J. Li, S. A. Cummer, Y. Jing, *Appl. Phys. Lett.* **2016**, *108*, 223502.

[17] B. Y. Xie, K. Tang, H. Cheng, Z. Y. Liu, S. Q. Chen, J. G. Tian, *Adv. Mater.* **2017**, *29*, 1603507.

[18] J. F. Li, C. Shen, A. Diaz-Rubio, S. A. Tretyakov, S. A. Cummer, *Nat. Commun.* **2018**, *9*, 1342.

[19] H. C. Tang, Z. S. Chen, N. Tang, S. F. Li, Y. X. Shen, Y. G. Peng, X. F. Zhu, J. F. Zang, *Adv. Funct. Mater.* **2018**, *28*, 1801127.

[20] Z. H. Tian, C. Shen, J. F. Li, E. Reit, Y. Y. Gu, H. Fu, S. A. Cummer, T. J. Huang, *Adv. Funct. Mater.* **2019**, *29*, 1808489.

[21] S. A. Cummer, J. Christensen, A. Alu, *Nat. Rev. Mater.* **2016**, *1*, 16001.

[22] G. C. Ma, P. Sheng, *Sci. Adv.* **2016,** *2*, e1501595.

[23] H. Ge, M. Yang, C. Ma, M. H. Lu, Y. F. Chen, N. Fang, P. Sheng, *Natl. Sci. Rev.* **2017,** *5*, 159–182.

[24] Y. Y. Fu, C. Shen, X. H. Zhu, J. F. Li, Y. W. Liu, S. A. Cummer, Y. D. Xu, *Sci. Adv.* **2020,** *6*, eaba9876.

[25] J. Qian, J. P. Xia, H. X. Sun, Y. Wang, Y. Ge, S. Q. Yuan, Y. H. Yang, X. J. Liu, B. L. Zhang, *Adv. Mater. Tech.* **2020**, 2000542.

[26] J. K. Weng, Y. J. Ding, C. B. Hu, X. F. Zhu, B. Liang, J. Yang, J. C. Cheng, *Nat. Commun.* **2020,** *11***,** 1-8.

[27] D. Wen, et al. *Nat. Commun.* **2015,** 6, 8241.

[28] W. Ye, F. Zeuner, X. Li, B. Reineke, S. He, C. W. Qiu, J. Liu, Y. Wang, S. Zhang, T. Zentgraf, *Nat. Commun.* **2016**, **7**, 11930.

[29] S. M. Kamali, E. Arbabi, A. Arbabi, Y. Horie, M. Faraji-Dana, A. Faraon, *Phys. Rev. X* **2017**, *7*, 041056.

[30] H. X. Xu, G. W. Hu, M. H. Jiang, S. W. Tang, Y. Z. Wang, C. H. Wang, Y. J. Huang, X. H. Ling, H. W. Liu, J. F. Zhou, *Adv. Mater. Tech.* **2020**, **5**, 1900710.

[31] S. Iqbal, H. Rajabalipanah, L. Zhang, X. Qiang, A. Abdolali, T. J. Cui, *Nanophotonics* **2020**, *9*, 703-714.

[32] K. Chen, G. Ding, G. Hu, Z. Jin, J. Zhao, Y. Feng, T. Jiang, A. Alu, C. W. Qiu, *Adv. Mater.* **2020**, *32*, e1906352.

[33] Y. F. Zhu, B. Assouar, *Phys. Rev. Mater.* **2019**, *3*, 045201.

[34] Y. F. Zhu, X. D. Fan, B. Liang, J. C. Cheng, Y. Jing, *Phys. Rev. X* **2017**, *7*, 021034.

[35] Y. F. Zhu, B. Assouar, *Phys. Rev. B* **2019,** *99*, 174109.

[36] Y. F. Zhu, S. W. Fan, L. Y. Cao, K. Donda, B. Assouar, *Phys. Rev. Appl.* **2020,** *14*, 014038.

[37] L. Kinsler, Fundamentals of Acoustics (Wiley, New York, 1982).

[38] Y. Li, X. Jiang, B. Liang, J. C. Cheng, L. K. Zhang, *Phys. Rev. Appl.* **2015**, *4*, 024003.

[39] M. H. Lu, X. K. Liu, L. Feng, J. Li, C. P. Huang, Y. F. Chen, Y. Y. Zhu, S. N. Zhu, N. B. Ming, *Phys. Rev. Lett.* **2007**, *99*, 174301.

[40] Y. Li, B. Liang, X. Y. Zou, J. C. Cheng, *Appl. Phys. Lett.* **2013**, *103*, 063509.

[41] N. J. Gerard, Y. Jing, *MRS Commun.* **2019**, *10*, 32-41.

[42] N. J. Gerard, Y. Li, Y. Jing, *J. Appl. Phys.* **2018,** *123*, 124905.

[43] X. Wang, X. Fang, D. Mao, Y. Jing, Y. Li, *Phys. Rev. Lett.* **2019,** *123*, 214302.

[44] G. Memoli, M. Caleap, M. Asakawa, D. R. Sahoo, B. W. Drinkwater, S. Subramanian, *Nat. Commun.* **2017**, *10*, 14608.

[45] N. J. Gerard, H. Cui, C. Shen, Y. Xie, X. Zheng, S. A. Cummer, Y. Jing, *Appl. Phys. Lett.* **2019**, *114*, 231902.

[46] M. M. Boone, E. N. G. Verheijen, T. Van, F. Peter, *J. Audio Eng. Soc.* **1995,** *43*, 1003.

[47] S. Zhang, L. L. Yin, N. Fang, *Phys. Rev. Lett.* **2009**, *102*, 194301.

[48] I. A. S. Elhelf, H. Albahar, U. Shah, A. Oto, E. Cressman, M. Almekkawy, *Diagn. Interventional Imaging* **2018**, *99*, 349.

[49] M. Duocastella, C. B. *Laser Photon. Rev.* **2012,** *6*, 607–621.

[50] C. Lee, J. S. Jeong, J. Y. Hwang, J. Lee, K. K. Shung, *Appl. Phys. Lett.* **2014,** *104*, 244107.